

Investigation of a fractured limestone cliff (Chartreuse Massif, France) using seismic tomography and ground-penetrating radar

Carine Dussauge-Peisser, Marc Wathelet*, Denis Jongmans, Didier Hantz, Bernard Couturier and Michel Sintès

LIRIGM, University Joseph Fourier, BP 53, 38041 Grenoble cedex 9, France

Received March 2003, revision accepted August 2003

ABSTRACT

Evaluating the stability state of a rock slope is a complex problem, mainly due to the lack of knowledge of the real state of the rock mass. Geophysical methods appear to be useful for investigating the deep discontinuity pattern, which may be poorly interpreted from surface observations. However, they have seldom been applied on steep rock slopes. The aim of this study is to test seismic tomography and ground-penetrating radar on near-vertical cliffs, and assess the quality of information that they can provide when investigating the characteristics of the fracture pattern inside the massif.

The test site is located in the Chartreuse massif, 20 km north-west of Grenoble, France. It is a 15 m high limestone cliff, characterized by one main near-vertical discontinuity set, including some wide open fractures.

Seismic tomography has been conducted between the vertical free surface and the plateau above, along three parallel profiles. Results show strong velocity gradients, from 800 to 3500 m/s. Some triangular low-velocity zones can be correlated with field observation of open fractures, but different tests on synthetic models and on real data show that the method is too sensitive to such heterogeneous conditions to provide accurate information on the fracture pattern.

Ground-penetrating radar surveys have also been acquired along vertical profiles on the cliff. We used three different antennae with centre frequencies of 35, 120 and 500 MHz. The penetration depth varied from 10 m (500 MHz) to about 20 m (35 MHz). The main reflectors are near-vertical and most of them can be correlated with fractures observed on the site. The reflectivity varies strongly along one single reflector, indicating changes in the aperture and/or filling characteristics.

INTRODUCTION

Natural hazards, such as rock falls and rock slides, are frequent phenomena in mountain areas like the Alps (Aleotti and Chowdury 1999). As urbanization is developing in such rock-fall prone areas, there is a growing need for new and reliable hazard assessment procedures (Ho *et al.* 2000). Evaluating rock-fall hazards means estimating the location, size and probability of occurrence of potential events during a given time, as well as the propagation of the unstable mass (Cancelli and Crosta 1993). Here we focus on the localiza-

tion and characterization of potential instabilities. Evaluating the stability state of a rock slope is a complex problem, mainly due to the number of possible failure mechanisms and to the lack of knowledge of the real present state of the rock mass (InterregIIc 2001). The location and size of potential rock falls are mainly dictated by the geometrical patterns and geomechanical properties of the rock mass, strongly influenced by existing discontinuities (e.g. Hoek and Bray 1981; Hudson 1992). The stability assessment is generally based on observations of the slope morphology as well as on a structural study of the massif, including measurements and characterization of the dis-

* marc.wathelet@ujf-grenoble.fr

continuities observed at the surface (e.g. Mazzoccola and Hudson 1996; Rouiller *et al.* 1998). However, even with the most accurate structural observations, the continuity of the fracture properties inside the rock mass is not guaranteed. This lack of information is one of the major problems for hazard assessment in rock-fall prone areas (Jaboyedoff *et al.* 1996; Crosta 1997).

In this regard, geophysical methods appear as suitable tools to acquire information about the internal state of the rock mass and to investigate the deep discontinuity pattern. However, up to now, these methods have seldom been applied to near-vertical cliffs or high natural rock slopes (Hack 2000), mainly due to the practical difficulties of performing tests on such sites. A few geophysical studies have been performed on steep slopes to detect and define potentially unstable masses, using mainly two methods: seismic tomography and ground-penetrating radar (GPR). During the last two decades, seismic tomography has proved to be an efficient tool to investigate rock masses (e.g. Ivanson 1987). While cross-hole tomography has been the most popular method, tomographic surveys where all sources and receivers are located on the ground surface are increasingly used (Lanz *et al.* 1998; Jongmans *et al.* 2000). On steep slopes, seismic imaging was applied by Zou and Wu (2001) in a quarry to investigate the blast-induced fracture in rock mass between the horizontal bench and the vertical wall, and by Jongmans and al. (2000) to assess the stability along railway slopes affected by a rock slide.

Based on the propagation of high-frequency electromagnetic waves, GPR is now widely used in engineering geology for shallow depth investigation (Reynolds 2000). In geological hazard assessment, the GPR method has proved to be suitable for locating superficial cavities (Benson 1995) and for mapping faults and fractures (Stevens *et al.* 1995; Demanet *et al.* 2001). Fracture detection with GPR in a given frequency range depends on the aperture and the filling of the discontinuities, which control the reflection coefficient (Grégoire 2001). Radar experiments in different rocks have shown that open and clay- or water-filled discontinuities are clearly visible when using appropriate wavelengths, while closed joints with no filling do not usually appear (Pettinelli *et al.* 1996; Hack 2000). This method then emerges as a major geophysical tool for estimating the continuity and distribution of fractures inside a rock mass, if this latter is not too conductive and attenuating. Pettinelli *et al.* (1996) obtained 6 m of penetration in unweathered limestone with clayey interbeds and marly sequences (where attenuation is important). A combination of GPR and seismic tomography was also used in a gypsum quarry in order to localize cracks and damage areas inside pillars (Derobert and Abraham 2000).

The present study, which is part of a project on rock-fall hazard assessment in the urban area of Grenoble, France

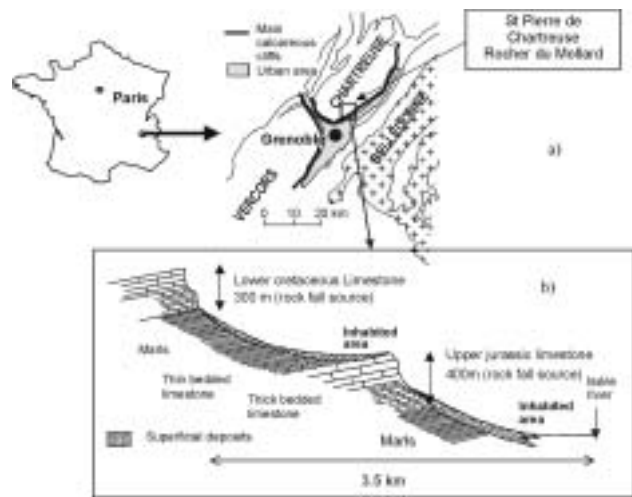


FIGURE 1 (a) Rock-fall hazard implication in the Grenoble urban area, France, and location of the “Rocher du Mollard” test site in the Chartreuse massif. (b) Typical cross-section of cliffs considered to present rock-fall hazards: two main near-vertical limestone formations are separated by marl layers.

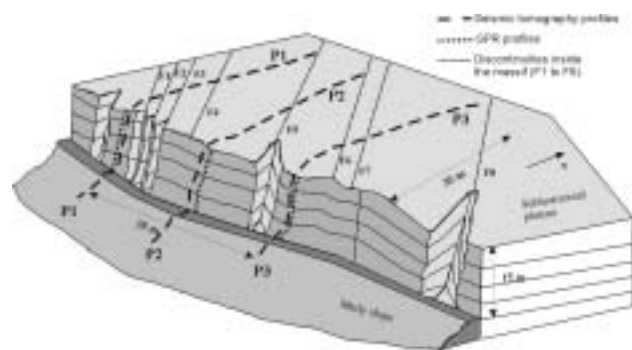


FIGURE 2 Schematic representation of the test site with a 15 m high limestone cliff. Location of the seismic tomography (P1 to P3) and GPR profiles and their intersection with the fractures (F1 to F8).

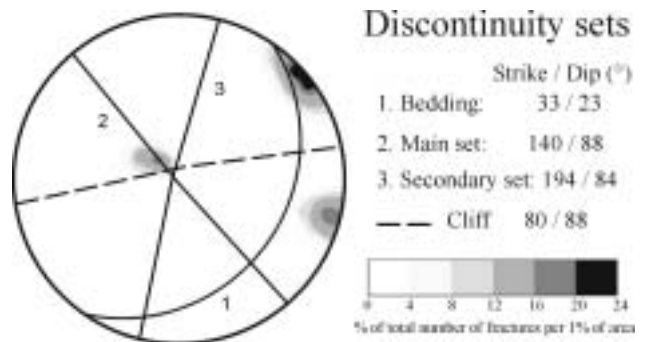


FIGURE 3 Wulf stereogram (upper hemisphere) for the structural analysis at the Rocher du Mollard site (31 pole measurements).

(SDAU 2001), aims at testing some geophysical methods on near-vertical limestone cliffs and at investigating the quality of information they can provide in this particular rock-slide prone area. A selection was made among the techniques usable on vertical cliffs, and the two methods previously used by other authors – seismic tomography and ground-penetrating radar – were applied in order to assess the internal geometrical and physical properties of the rock cliff. Electrical tomography was discarded due to the difficulty in setting electrodes in limestone and in ensuring a good electrical coupling. Geophysical experiments were performed on one test site and results are validated with geological and structural data.

THE STUDY SITE

The Grenoble region is subject to a high risk of rock fall (SDAU 2001) because of the existence of high calcareous cliffs (up to 400 m) located above inhabited areas (Fig. 1a). These cliffs are part of the Chartreuse and Vercors massifs (sub-Alpine chains), culminating above 2000 m and made of sedimentary rocks (limestone and marls) from upper Jurassic to lower Cretaceous age (Fig. 1b). The “Rocher du Mollard” study site is a near-vertical limestone cliff, 10 to 15 m high, located in the Chartreuse massif, 20 km north-west of Grenoble, near the village of St Pierre de Chartreuse. This site does not present any specific rock-fall hazard and has been chosen mainly for its accessibility and for the simplicity of its geological structure. The cliff, which strikes N80°, is made of Tithonian limestone, lying on a marly layer of the Kimmeridgian age (Fig. 2). The surface at its top is a near-horizontal plateau (Fig. 2), showing scattered limestone outcrops on the first few metres near the cliff. A structural study of the site (Dussauge-Peisser 2002) has shown that the limestone mass is affected by three main discontinuity sets: the bedding and two fracture families, whose poles are shown on a stereographic projection in Fig. 3. The bedding dips gently (N33°E/23°NW) to the inside of the massif, while the two fracture sets are near-vertical. The main discontinuity set (denoted 2 in Fig. 3) strikes N140°E, i.e. at an angle of 60° with the cliff orientation. Within this set, three fractures are wide open near the cliff (F3, F5 and F8 on Fig. 2), but their further extension into the massif is poorly visible, due to covering material and vegetation on the plateau. F5 is the widest fracture on the site, being 2–4 m open with a filling of limestone blocks and clayey material. F8 lies at the border of the test site and does not cross the measured profiles. Five other discontinuities appear more or less open on the cliff wall (F1, F2, F4, F6 and F7 in Fig. 2). F1, F2 and F6 appear to close rapidly on the plateau behind the cliff, while F4 remains visible. On the cliff, F7 appears to be closed at the top of the cliff wall but it is open 2 m under the plateau. The secondary set (set 3 in Fig. 3) does not present any open discontinuity.

The presence of the upper weathered layer and of karstic phenomena within the limestone lowers the penetration of radar waves. Preliminary tests performed on the plateau showed a maximum penetration of 2–3 metres with a 120 MHz antenna. Moreover, the main open discontinuities are near-vertical and are poorly imaged by horizontal profiles. For these two reasons, GPR vertical sections were measured with antennae placed directly on the cliff. This layout avoids the conductive weathered layer and allows reflections from the main vertical discontinuities observed on the cliff to be recorded. Seismic tomography experiments were conducted between the vertical free surface and the plateau above, along three parallel profiles (labelled P1 to P3 in Fig. 2), at the same locations as the radar sections. As the test site is highly heterogeneous, with *a priori* high-velocity contrasts, the aim of the study is also to test the limits of the seismic tomography method under such conditions.

SEISMIC TOMOGRAPHY

During the experiments, receivers were distributed along the whole length of the profile lines (P1, P2 and P3 in Fig. 2). For practical purposes, source positions were only placed on the plateau and on the lower marly slope. With this layout, the resolution, which mainly depends on the ray coverage, is generally good in the triangle crossed by the rays (Ivanson 1987). First-arrival times are picked on all recorded traces and are inverted using the simultaneous iterative reconstruction technique (Dines and Lytle 1979) implemented with a 3D software for refraction and tomography analysis (Demanet 2000). A first seismic image is necessary as a starting point for inversion and is obtained using either the back-projection technique (Lager and Lytle 1977), or a homogeneous model with a constant velocity value, or a layered model with a lower velocity for the marly level. From synthetic studies, Demanet (2000) showed that the final image is smooth and generally insensitive to the starting model, except in unfavourable situations where *a priori* information is necessary to discriminate between different solutions. In order to estimate the resolving power of the method in our case study, a synthetic model close to the expected geological situation at the Mollard site is first analysed using a field survey layout.

Synthetic models

The models used in the computation are shown in Figs 4a and 5a. The topography and survey layout are similar to profile P1 (Fig. 2). The limestone (assumed P-wave velocity of 3500 m/s) is overlain by a 2 m thick weathered layer (P-wave velocity of 500 m/s). In the second model (Fig. 5), the marly level at the base of the cliff is also considered. This has a velocity of 1800 m/s and an apparent dip of 16° (the bedding dip is 23° and the angle between the bedding and the plane of the profile is 43°). In order to test the potential of the

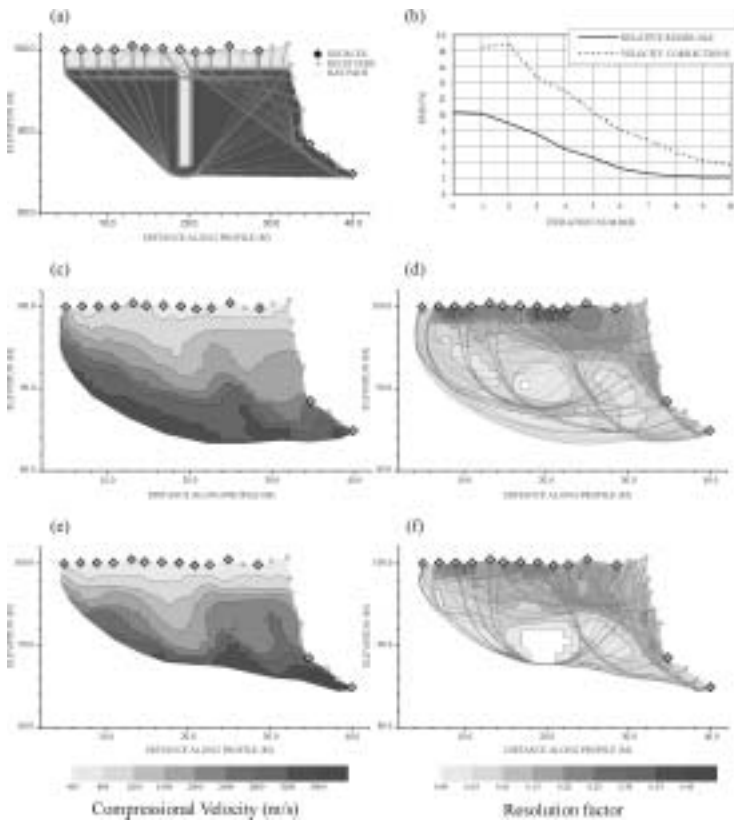


FIGURE 4

First synthetic model for the seismic tomography method. (a) Original model with a vertical discontinuity (1 m thick, 12 m deep, 500 m/s) in a homogeneous medium (3500 m/s) overlain by a 2 m thick weathered layer of 500 m/s. (b) Convergence history for time residuals and velocity corrections. (c) and (e) Seismic velocity images, (d) and (f) the corresponding resolution factors, after 5 and 10 iterations, respectively.

technique to detect vertical fractures, a 1 m thick vertical low-velocity zone (500 m/s) was introduced into the model (Figs 4 and 5). The P-wave velocity values were chosen from refraction test results and the thickness value is consistent with the geological observations at the surface.

The theoretical propagation times (forward modelling) were computed for these models (without and with the marly layer) and the corresponding raypaths are shown in Figs 4a and 5a, respectively. These time data were inverted. The relative root-mean-square (RMS) is defined as

$$RMS = \sqrt{\frac{\sum_{i=1}^n \left(\frac{t_{ci} - t_{mi}}{t_{ci}} \right)^2}{n}}, \quad (1)$$

where t_m and t_c are the measured and calculated arrival times, respectively, and n is the total number of rays. An absolute RMS value can be calculated using the same equation without dividing the time residuals by t_c . Another statistic used is the RMS of velocity corrections, which is given by (1), with t_m and t_c replaced by V_{j-1} and V_j , respectively (j is the iteration number and n is the number of grid cells).

In model 1, the velocity and resolution factors obtained after 5 and 10 iterations are shown in Figs 4c–4f, starting from a homogeneous model with velocity 4500 m/s. The resolution image is obtained by plotting the normalized diagonal of

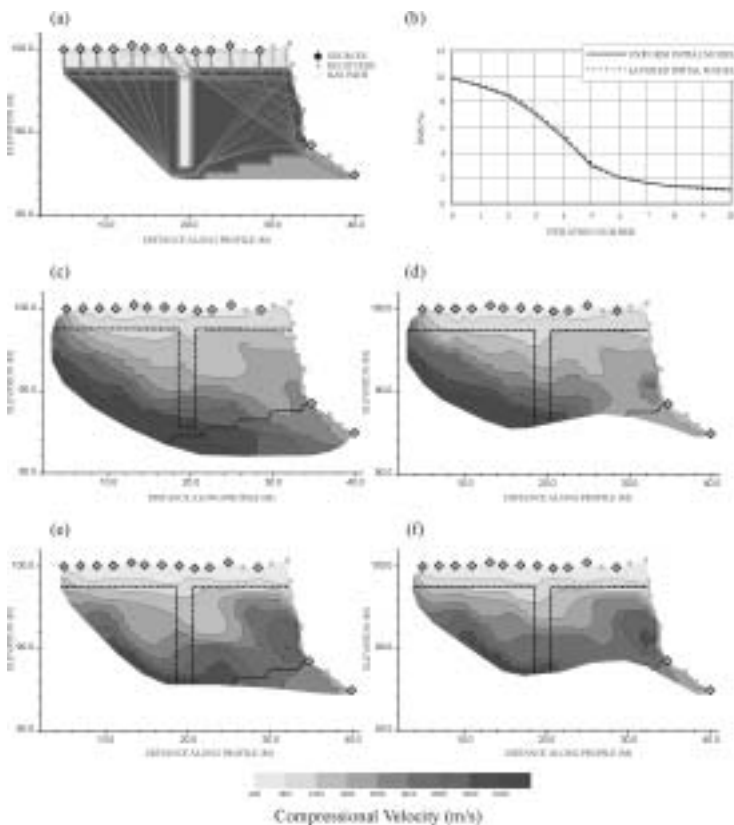


FIGURE 5

Second synthetic model for the seismic tomography method. (a) Original model with a vertical discontinuity (1 m thick, 12 m deep, 500 m/s) in a layered medium (massive limestone of 3500 m/s under a 2 m thick weathered layer of 500 m/s and over a marly layer of 1800 m/s, with an apparent dip of 16°). (b) Convergence history for relative time residuals starting from a uniform initial model or a layered initial model. (c) and (e) Seismic velocity images starting from a uniform initial model of 4500 m/s after 5 and 10 iterations, respectively. (d) and (f) Seismic velocity images starting from a layered initial model (4500 and 1800 m/s) after 5 and 10 iterations, respectively.

the resolution matrix (Ivanson 1987). The development of the relative RMS values and the velocity corrections with the number of iterations is shown in Fig. 4b. Both curves decrease continuously and relative RMS values of around 5% and 2% are reached after 5 and 10 iterations, respectively. At this later stage, the velocity values in the lower bedrock (3500 m/s) and in the cap weathered layer (500 m/s) are correctly retrieved (Fig. 4e). On the other hand, the boundary between the two layers is not seen, due to the smoothing resulting from the inversion process. The crack is marked by a low-velocity zone with a triangular shape. The resolution factor (Figs 4d and 4f) is good in the upper part of the section while it is poor in the basal part, especially at the crack location which is by-passed by the ray trajectories. On the image obtained after 5 iterations (Fig. 4c), the crack is less visible and slightly affects the iso-velocity lines. Some low-velocity anomalies, probably resulting from the artefact due to the poor azimuthal ray coverage, appear behind the cliff and at the end of the profile.

When considering the effect of the marly level at the base of the cliff (Fig. 5), results are globally similar, with some new features appearing. The slow zone is wider and the position of the vertical fracture is not very precise. The precision increases with the number of iterations, Figs 5e and 5f after 10 iterations being more accurate than Figs 5c and 5d after 5 iterations. The importance of the *a priori* information included in the inversion model is highlighted with Figs 5d and 5f where the initial model is layered. The location of the slow zone is slightly more precise. The velocity of the marly layer (1800 m/s) appears near the surface at the foot of the slope. Another important feature is the higher velocity zone (>3200 m/s) which appears after 10 iterations near the cliff surface, corresponding to the limestone velocity. The relative RMS values are very similar for both initial models (Fig. 5b) and fall to very low values, respectively 3.1% and 1% after 5 and 10 iterations.

With the layout used and the geometry of the investigated geological structure, seismic images are smoothed compared to the theoretical model, and the fracture location is shown by a triangular low-velocity zone. The solution is not unique, as shown in Fig. 5 with low RMS values characterizing different images.

Field data results

All signals were recorded using a Bison seismograph connected to 24 vertical geophones (4.5 Hz) fixed every two metres on the plateau, on the cliff (using metallic angles) and on the lower marly slope. Exact positions were measured with a theodolite with an error of less than 1 cm. Waves were generated by a sledge hammer and shot source points were located on the plateau and on the marly slope. The seismograms and the picked times for one endshot are shown in Fig. 6, as well as the Fourier transform of one of the

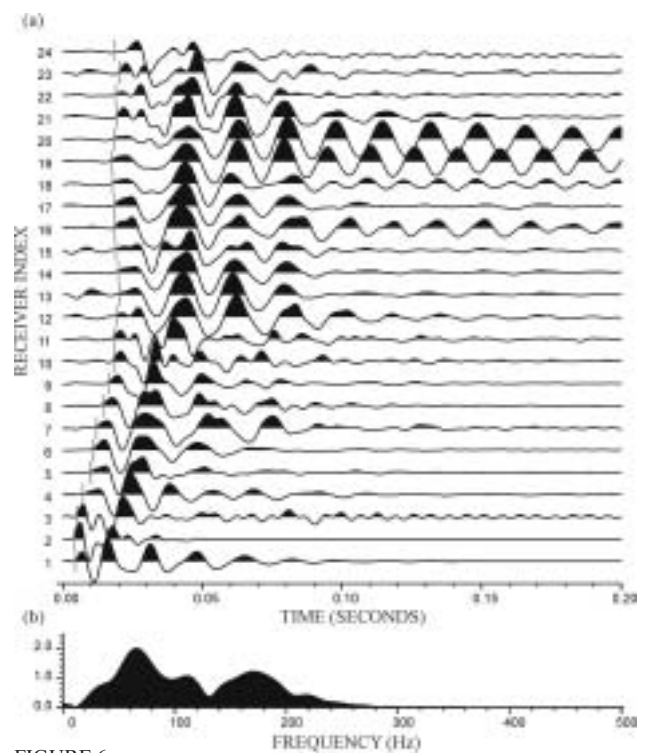


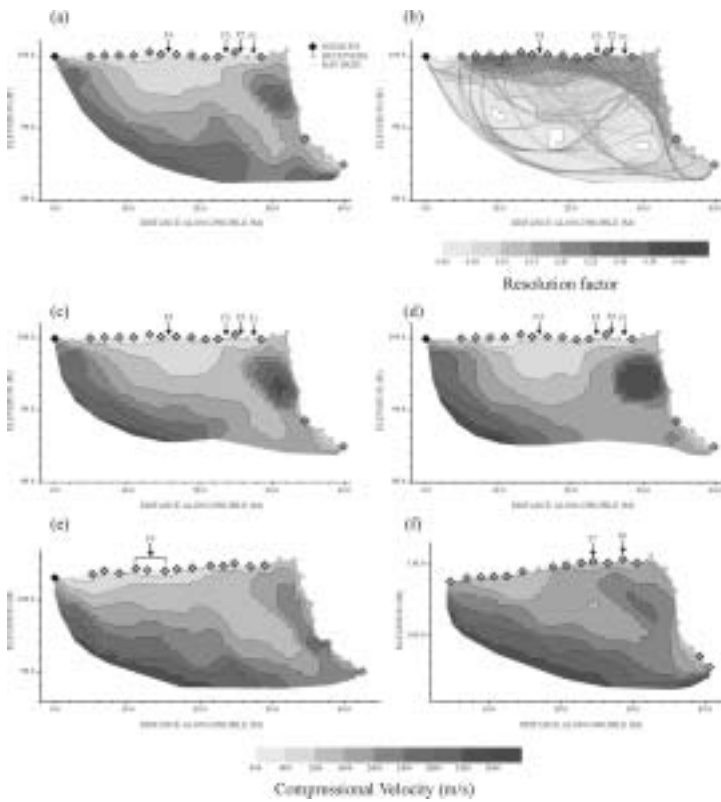
FIGURE 6

(a) Profile 1, seismograms recorded at the 24 receivers for a source located on the plateau at distance 0.0 m (Fig. 7). (b) Fourier transform of signal 2.

signals. Seismic energy ranges from 20 Hz to 250 Hz. P-wave velocity images for the three profiles are shown in Fig. 7, as well as the resolution and the raypaths in one case (Fig. 7b).

For profile 1, when starting with a homogeneous model of 4500 m/s, the inversion reaches a relative RMS of 4.3% after 7 iterations (Fig. 7a). It is characterized by a low-velocity zone (800 to 1600 m/s) with a triangular shape in the middle of the section, extending behind the cliff and associated with a vertical high-velocity zone (1600 to 2800 m/s). The introduction of a *a priori* information on the lower-velocity marly level does not greatly modify the image (Fig. 7c) and slightly lowers the RMS value (3.7%). Finally, the image of Fig. 7c where the low-velocity zone has been removed was used as a starting model and the final image, obtained with a RMS of 3.6%, is shown in Fig. 7d. This suggests that a low-velocity zone behind the cliff is not essential to explain the data, even if a similar shape is seen on all profiles (Figs 7a, 7e and 7f). On all these profiles the highest values in the limestone are between 3200 and 3600 m/s and the sections exhibit a high-velocity contrast (from less than 800 m/s to 3600 m/s) between different zones.

The convergence history for the three sections is shown in Fig. 8. Profiles 1 and 2 show low relative RMSs (less than 5%) with good resolution on a thickness varying from 5 to 10 metres after 7 and 5 iterations, respectively. For the third profile, the model exhibits the same global shape as the



other two, with a higher relative RMS value (8.7%) and poor resolution in the central part of the image. The increase in the relative RMS for profile 3 is not very surprising as the absolute RMS is used for convergence. On the three profiles, the velocity values decrease (1200 to 2000 m/s) on the marly slopes. Different starting models were tested in the inversion and the final image obtained appeared to be stable for the three seismic sections.

The images provided along the three profiles show some low-velocity zones (800 m/s at the surface) extending to depth, which are comparable to the anomalies created by vertical fracture zones (cf. Figs 4e and 7). The similarity to synthetic images is, however, far better when considering the influence of the marly layer (compare the high-velocity zone parallel to the cliff and the low-velocity zone at the surface of the marly talus in Figs 5e/f and 7). On Profile 1, the central low-velocity zone can be correlated with fracture observations in the field. The deepest part of the near-surface low-velocity zone (800–1200 m/s) is located at a distance of 14–16 m along the profile, which corresponds to the intersection of the profile with the open discontinuity F4 in Fig. 2. Closer to the cliff, the discontinuities F1, F2 and F3 (Fig. 2) intersect Profile 1 between 24 m and 28 m (distance measured along profile), where the seismic image shows a significant horizontal gradient (from 3500 m/s near the cliff to 1600 m/s). In tomograms for P2 and P3, the influence of the known discontinuities is not detected. The low-velocity zone is very wide on Profile 2 where the large fracture F5 is expected. On Profile 3, no particular low-velocity zone appears where the discontinuities F6 and F7 are

FIGURE 7

Results of the seismic tomography for the field data. (a) Profile 1 (homogeneous initial model of 4500 m/s) and (b) the associated resolution image, after 7 iterations, relative RMS=4.8%. (c) Profile 1, starting from a layered model, after 7 iterations, relative RMS=3.7%, and (d) starting from the modified image of Fig. 7c (see text), relative RMS=3.6%. (e) Profile 2, homogeneous initial model, 5 iterations, relative RMS=3.8%. (f) Profile 3, homogeneous initial model, 4 iterations, relative RMS=8.7%. Arrows indicate the locations of the observed discontinuities along the profiles.

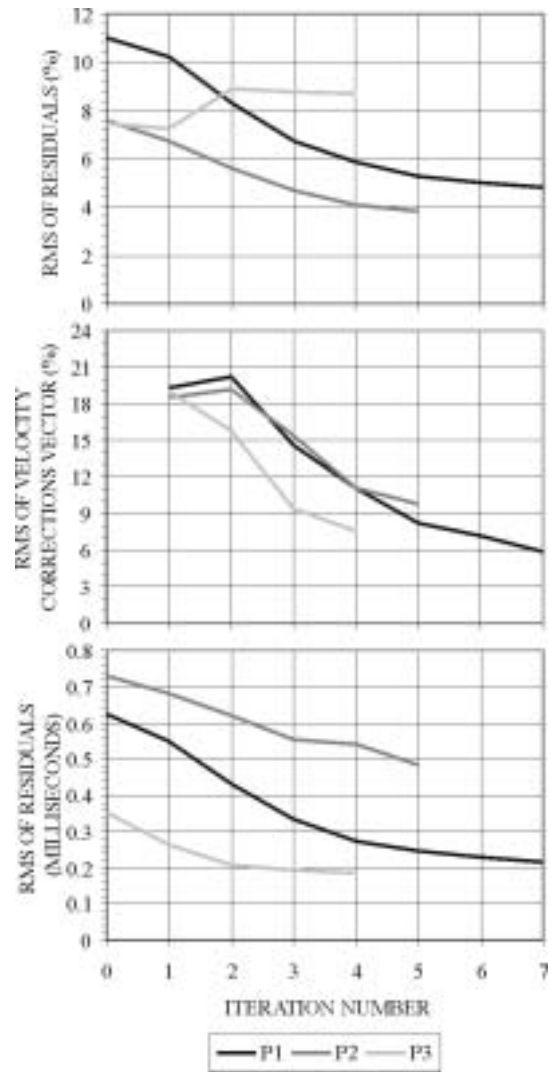


FIGURE 8

Convergence history for time residuals and velocity corrections for the three seismic profiles, starting from a homogeneous initial model.

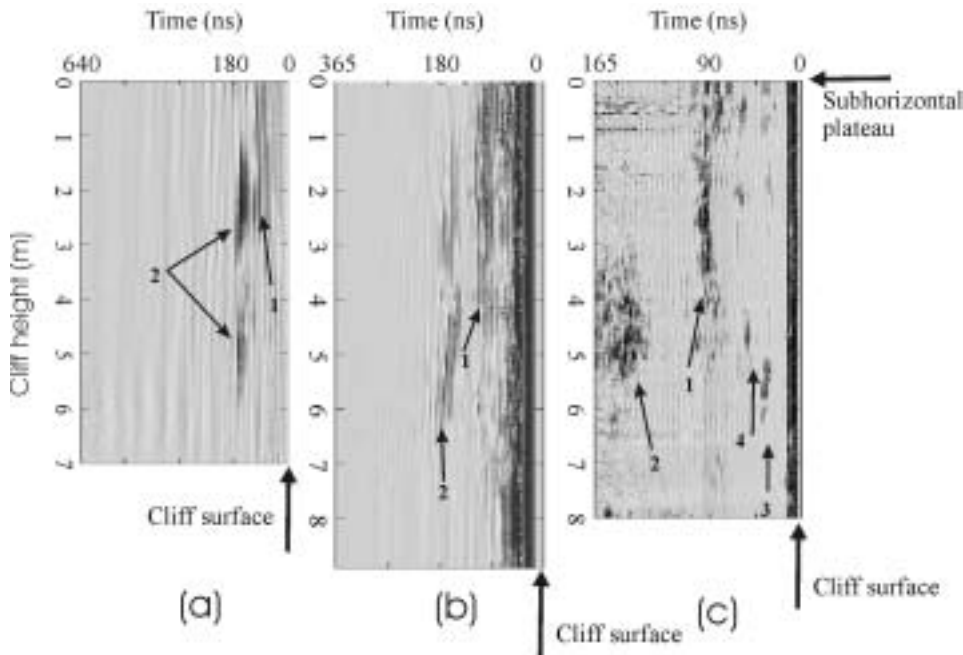


FIGURE 9
GPR profiles measured along P1 with (a) 35 MHz antenna, (b) 120 MHz antenna, (c) 500 MHz antenna. Arrows indicate the four main reflectors referred to in the text.

expected to intersect the section. A lower signal-to-noise ratio observed on profile 3 and/or three-dimensional effects are thought to explain this situation, and is supported by the high RMS value (8.7%). The deepening of the low-velocity zone just behind the cliff on the three images has to be considered in the light of Fig. 7d. It can be linked to the device layout used in this study as suggested in Fig. 5f. However, the effect is much more visible on real images than on synthetic models and it could result from a difference of fracturing or weathering in the vicinity of the cliff. This item will be discussed below.

GROUND-PENETRATING RADAR (GPR)

Principle and layout

Three different GSSI monostatic antennae (35 MHz, 120 MHz and 500 MHz) were used on the Mollard site in order to test the penetration and resolution capacities of the method. One person drove the antennae vertically into the cliff, using ropes to secure it from the top, while a second person abseiled to guide and ensure a good contact with the rock. The acquisition centre remained on the plateau. With such a layout, each profile, around 10 m high, took about half an hour.

Results

The GPR sections for profile P1 are shown in Fig. 9. The main reflectors are near-parallel to the investigated surface, i.e. the vertical cliff. As the predominant fractures on this site are near-vertical, these reflectors probably correspond to these discontinuities. The three images obtained with different antennae provide information at different scales

and resolutions. The 35 MHz, 120 MHz and 500 MHz antennae revealed two main reflectors (labelled 1 and 2 in Fig. 9), recorded around 100 and 170 ns (two-way traveltime (TWT)), respectively. For all frequencies no reflections were detected at TWTs > 180 ns. With the 500 MHz antenna, these two reflectors are more precisely located at 90 and 160–165 ns, respectively; moreover two other reflectors (labelled 3 and 4, at 40 and 50 ns, respectively) appear closer to the cliff surface. For all antennae, large differences in reflectivity are clearly visible along the reflectors. In particular, reflector 1 which is clearly visible at 90 ns in the upper part of the cliff (Fig. 9c) tends to disappear at a depth of 5 m. Though visible on the whole section, reflectors 3 and 4 exhibit bright spots at specific depths. Reflector 2, which is visible on all sections, shows reflectivity patterns varying with frequency.

Radar sections measured with the 120 MHz antenna for the three profiles are shown in Fig. 10 as a function of depth. The radar wave velocity was estimated at 0.12 m/ns from the diffraction hyperbola, in accordance with published values for limestone (Hack 2000; Reynolds 2000). This velocity represents a mean value, since it can vary depending on clay content and on pore water content. Using this velocity, a 100 ns TWT represents 6 m of penetration. In this way, the main two reflectors on profile 1 (Fig. 10a) are located 5–6 m and 8–9 m from the cliff, respectively. They correspond in the field to the locations of the two open fractures F3 and F4 (Fig. 2), when the distance is measured orthogonally to the discontinuity orientation (Fig. 11). Discontinuities F1 and F2, closer to the cliff, are not visible on the 120 MHz section, due to the lack of resolution, but F1 can be correlated with reflector 4 on the 500 MHz section (Figs 9c and 12a).

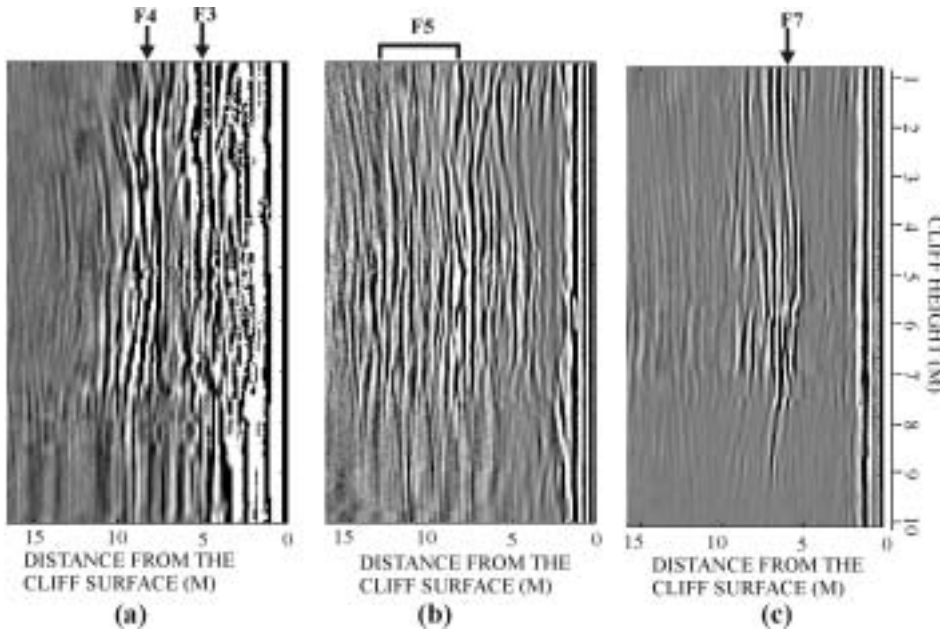


FIGURE 10
GPR profiles measured along (a) P1, (b) P2 and (c) P3 with the 120 MHz antenna. Arrows indicate the intersection of the radar profile with discontinuities observed on the site.

On profile 2 (Fig. 10b), several reflectors are evident at 8–12 m from the cliff. They appear to correspond to the wide fracture F5, even if multiple reflections are probably present. A first reflector, appearing at about 4 m from the cliff, is not correlated with any fracture observed on the field. Profile 3 (Fig. 10c) shows one predominant reflector 5–6 m from the cliff, with a higher reflectivity in the middle than at the top or at the bottom of the section. This reflector corresponds well to the discontinuity F7 (cf. Fig. 2). On the other hand, the discontinuity F6, which is closed at the outcrop, barely appears on the radar section.

In conclusion, the main reflectors revealed by the GPR method correspond roughly to the main open discontinuities observed on the site. However, some reflectors are not correlated to field observations, such as, for example, the

first reflector at 4 m from the cliff on profile 2. In this case, higher values of reflectivity are observed in the middle of the section, suggesting the presence of an open fracture at depth, which may be not visible at the surface. Such reflectivity variations along the cliff height are systematically seen on all profiles, indicating spatial changes of fracture characteristics (aperture and/or fill materials). Most significant is the systematic decrease in reflectivity values observed at the bottom of the cliff which becomes more marly in its lower part. Maximum penetration depth with the 120 MHz antenna is 10 m to 15 m.

COMPARISON OF THE TWO METHODS AND DISCUSSION

The 500 MHz and 120 MHz GPR sections for profile 1 are superposed on the corresponding tomographic seismic velocity image in Figs 12a and 12b, respectively. The horizontal distance scale of the GPR sections has been divided by $\cos 60^\circ$ to take into account the orientation of the main fracture set, relative to the seismic profile (Fig. 11). With this transformation, both sections may be considered orientated perpendicular to the cliff. The discontinuities observed on the cliff (Fig. 2) have also been shown in Fig. 12 at their estimated intersection with the 2D section (distance d on Fig. 11). Figure 12 shows the overall consistency between the different data sets. The two main open fractures (F3 and F4) visible at the surface are highlighted, first by radar reflections (1 and 2) at both frequencies and secondly by low seismic velocity anomalies. The other two discontinuities F1 and F2, less open at the surface, seem to be linked to reflectors 4 and to a branch of reflector 1 which divides near the surface.

Extending the results of profile 1 to the other two profiles, the presence of a radar reflector at about 4–5 m from

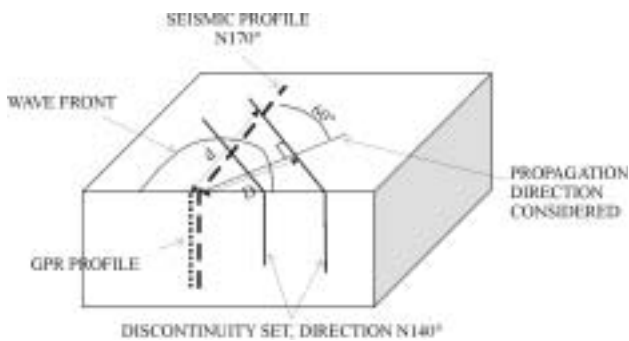
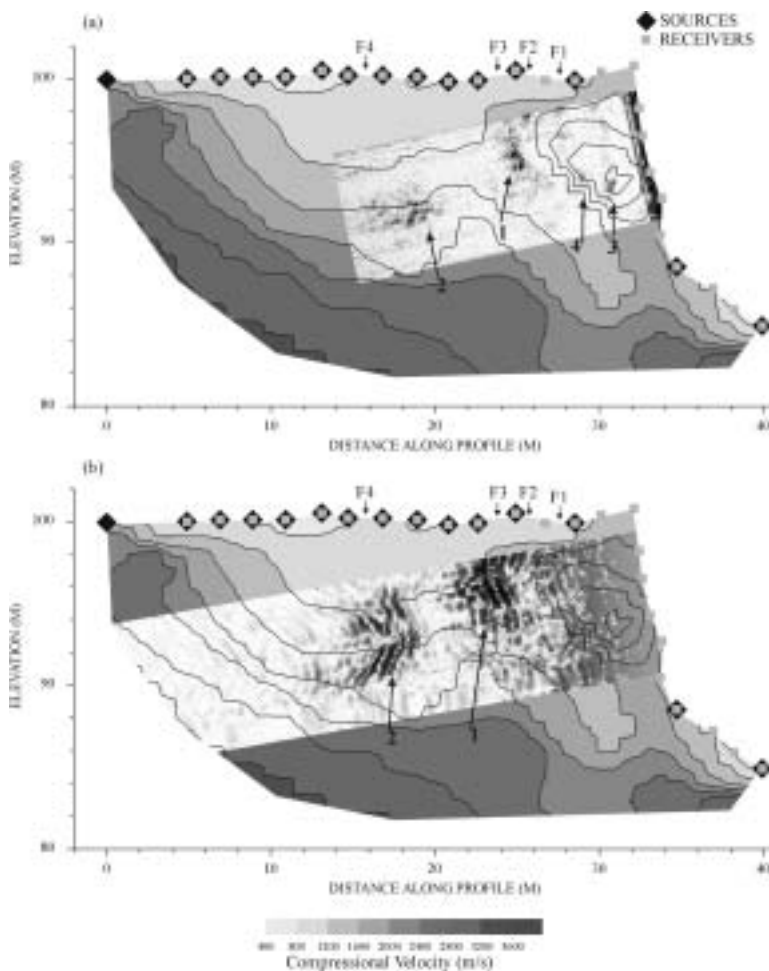


FIGURE 11
Schematic representation of the convention adopted to measure the distance of the discontinuities from the cliff surface. On the seismic tomography section, d is measured along the profile, i.e. orthogonally to the cliff surface. On the GPR section, D is measured orthogonally to the main discontinuity set. Thus, for the same fracture, $d = D/\cos 60^\circ$.



the cliff on the three profiles suggests the existence of a fractured zone at such a distance (corresponding to discontinuities F2 and F3 on profile 1). This hypothesis is corroborated by the presence of a horizontal velocity gradient behind the cliff on the seismic images.

Figure 12 also illustrates the difference in resolution of the two methods. While GPR allows the accurate detection of fractures, seismic sections are considerably smoothed and yield images which can be far from reality; this is demonstrated by the inversion of synthetic models. The open fractures are not precisely located with this method, but could be indicated by triangular low-velocity zones, more or less centred on the fracture. This results from the resolution of the method (estimated to be 2.5 m if taken to be a quarter of the wavelength for a velocity of 2000 m/s and a frequency of 200 Hz, cf. Fig. 6), the relatively poor ray-azimuthal coverage, the sharp velocity contrasts between fractured zones and limestone, and the inversion process itself. On the other hand, the presence of a thick layer whose velocity, low at the surface, increases with depth is supported by the observation of karstic phenomena (lapiés) on the limestone plateau, which result from intensive weathering propagating

FIGURE 12

Comparison between the results of seismic tomography and GPR on profile 1 with (a) 500 MHz antenna, (b) 120 MHz antenna. Arrows indicate the intersection of the seismic tomography profile with discontinuities observed on the site.

to depth through the fracture sets. Finally, inversions of synthetic models show that the lower and upper limits of the seismic velocity values are correct and the velocity contrast is surprisingly high (800 m/s to 3500 m/s) on these cliffs. These results must be considered as preliminary and other acquisitions must be performed and if possible validated by separate data in order to estimate the reliability of such images.

CONCLUSIONS

Two geophysical techniques (seismic tomography and GPR) were used on a 15 m high limestone cliff close to Grenoble, with the aim of developing investigation methods to evaluate the stability of near-vertical cliffs. Seismic tomography, applied between the cliff and the horizontal plateau, investigated a triangular zone, 34 m by 15 m. GPR sections were measured on vertical profiles with antennae placed on the cliff, in order to avoid the conductive weathered layer covering the plateau. Under these conditions, radar wave penetration in limestone reaches 15 to 20 m with 120 and 35 MHz antennae, respectively. The GPR method provided information on the location and the geometry of near-vertical fractures and appears to be a very promising tool for limestone cliff investigation. Of particular interest is the reflectivity variation along the same discontinuity, indicating changes in aperture and/or filling characteristics. On the other hand, the seismic tomography gave access to more global rock properties, through an image of seismic velocity. The measured images show strong velocity gradients (800 to 3500 m/s over a few metres) and are very similar to those obtained with synthetic models in which fractures give rise to low-velocity zones. The extreme values are correctly retrieved and some of the low-velocity zones can be correlated with observed fractures (F4 on profile 1, for instance). However, smoothing of the inversion process and the poor resolution significantly modify the shape of the anomalies. Moreover, the presence of a lower-velocity marly layer at the base of the cliff clearly affects the image, creating additional artefacts. Nevertheless, the comparison of all data (seismic, GPR and structural measurements) is consistent for profile 1, assuming that the radar waves are reflected by the main fracture

set observed in the field. These results highlight the power of the GPR method in characterizing the discontinuity pattern inside a rock mass, while the seismic images are smooth and insensitive in such heterogeneous conditions, leading to different possible solutions and preventing an accurate location of fractures in the massif.

Future developments of such studies include the improvement of GPR measurement procedures on cliffs in order to determine the orientation and location of reflectors, for instance by performing both horizontal and vertical profiles along the cliff. Also, with the relatively high penetration of radar waves found in this study, transmission tomography between the plateau and the cliff can be considered. Finally, in these GPR experiments, information from the reflection amplitudes at different frequencies was not exploited. Inversion of these data could give an insight into the thickness and the filling of the discontinuities reflecting the waves. This is highly important and is necessary to improve our knowledge about the inner geometry of fractures which control rock mass instabilities.

ACKNOWLEDGEMENTS

We thank R. Guiguet, H. Havenith, M. Jeannin, H. Teerlynck, J.M. Vengeon for their active participation in the field measurements and S. Garembois for his fruitful comments on the GPR results. This study was supported by the Regional Natural Park of Chartreuse and the Pôle Grenoblois des Risques Naturels.

REFERENCES

- Aleotti P. and Chowdury R. 1999. Landslide hazard assessment: summary review and new perspectives. *Bulletin of Engineering Geology and Environment* **58**, 21–44.
- Benson A.K. 1995. Applications of ground-penetrating radar in assessing some geological hazards: examples of groundwater contamination, faults, cavities. *Journal of Applied Geophysics* **33**, 177–193.
- Cancelli A. and Crosta G. 1993. Hazard and risk assessment in rock-fall prone areas. In: *Risk and Reliability in Ground Engineering* (ed. S. Bo), pp. 177–190. Thomas Telford, London.
- Crosta G. 1997. Evaluating rock mass geometry from photographic images. *Rock Mechanics and Rock Engineering* **30**, 35–58.
- Demanet D. 2000. *Tomographie 2D et 3D à partir de mesures géophysiques en surface et en forage*. PhD thesis, University of Liège.
- Demanet D., Renardy F., Vanneste K., Jongmans D., Camelbeeck T. and Meghraoui M. 2001. The use of geophysical prospecting for imaging active faults in the Roer graben, Belgium. *Geophysics* **66**, 78–89.
- Derobert X. and Abraham O. 2000. GPR and seismic imaging in a gypsum quarry. *Journal of Applied Geophysics* **45**, 157–169.
- Dines K. and Lyttle J. 1979. Computerized geophysical tomography. *Proceedings of the IEEE* **67**, 1065–1073.
- Dussauge-Peisser C. 2002. *Evaluation de l'aléa éboulement rocheux; Développements méthodologiques et approches expérimentales*. PhD thesis, University of Grenoble.
- Grégoire C. 2001. *Fracture characterisation by ground-penetrating radar*. PhD thesis, Katholieke University of Leuven.
- Hack R. 2000. Geophysics for slope stability. *Surveys in Geophysics* **21**, 423–448.
- Ho K., Leroi E. and Roberts B. 2000. Quantitative risk assessment: application, myths and future direction. In: *GeoEng2000*, Vol. 1. Technomic Publishing Co., Melbourne.
- Hoek E. and Bray J.W. 1981. *Rock Slope Engineering*. Elsevier Science Publishing Co.
- Hudson J.A. 1992. *Rock Engineering System: Theory and Practice*. High Plain Press (JAH).
- Interreg_IIC. 2001. *Prévention des mouvements de versant et des instabilités de falaise - Groupe Falaise - Confrontation des méthodes d'étude des éboulements rocheux dans l'arc alpin*. Programme Interreg IIC, Méditerranée occidentale et Alpes latines. Internal report, Grenoble.
- Ivanson S. 1987. Crosshole transmission tomography. In: *Seismic Tomography with Applications in Global Seismology and Exploration Geophysics* (ed. G. Nolet), pp. 159–188. Reidel Publishing Company.
- Jaboyedoff M., Philipposian F., Mamin M., Marro C. and Rouiller J.D. 1996. *Distribution spatiale des discontinuités dans une falaise. Approche statistique et probabiliste*, Final Report PNR31, VDF, Zürich.
- Jongmans D., Hemroulle, P., Demanet, D., Renardy, F. and Vanbrabant, Y. 2000. Application of 2D electrical and seismic tomography techniques for investigating landslides. *European Journal of Environmental and Engineering Geophysics* **5**, 75–89.
- Lager D.L. and Lyttle R.J. 1977. Determining a subsurface electromagnetic profile from high frequency measurements by applying reconstruction technique algorithms. *Radio Science* **12**, 249–260.
- Lanz E., Maurer H. and Green A.G. 1998. Refraction tomography over a buried waste disposal site. *Geophysics* **63**, 1414–1433.
- Mazzoccola D. and Hudson J.A. 1996. A comprehensive method of rock mass characterization for indicating natural slope instability. *The Quarterly Journal of Engineering Geology* **29**, 37–56.
- Pettinelli E., Beaubien S. and Tommas P. 1996. GPR investigations to evaluate the geometry of rock slides and buckling in a limestone formation in northern Italy. *European Journal of Environmental and Engineering Geophysics* **1**, 271–286.
- Reynolds J.M. 2000. *An Introduction to Applied and Environmental Geophysics*. John Wiley & Sons, Inc.
- Rouiller J.D., Jaboyedoff M., Marro C., Philipposian F. and Mamin M. 1998. *Pentes instables dans le Pennique valaisan. MATTE-ROCK: une méthodologie d'auscultation des falaises et de détection des éboulements majeurs potentiels*. Final Report PNR31, VDF, Zürich.
- SDAU 2001. *Etude des aléas majeurs d'écroulement rocheux sur les falaises calcaires du Y grenoblois*. In: *Rapport d'étape du syndicat mixte pour l'élaboration et le suivi du Schéma Directeur d'Aménagement et d'Urbanisme de l'agglomération Grenobloise*. Internal report, Grenoble.
- Stevens K.M., Lohda G.S., Holloway A.L. and Soonawala N.M. 1995. The application of ground-penetrating radar for mapping fractures in plutonic rocks within the Whiteshell Research Area, Pinawa, Manitoba, Canada. *Journal of Applied Geophysics* **33**, 125–141.
- Zou D.H. and Wu Y.K. 2001. Investigation of blast-induced fracture in rock mass using reversed vertical seismic profiling. *Journal of Applied Geophysics* **48**, 153–169.